Applied Energy 359 (2024) 122680

Contents lists available at ScienceDirect

Applied Energy

journal homepage: www.elsevier.com/locate/apenergy

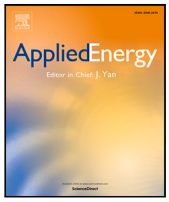

A Rheo-Impedance investigation on the interparticle interactions in the catalyst ink and its impact on electrode network formation in a proton exchange membrane fuel cell

Shirin Mehrazi [a], Taymaz Homayouni [b], Nitul Kakati [b], Mrittunjoy Sarker [b], Philip Rolfe [c], Po-Ya Abel Chuang [a,b,*]

[a] Environmental Systems Graduate Group, University of California, Merced, CA 95343, United States
[b] Department of Mechanical Engineering, University of California, Merced, CA 95343, United States
[c] Netzsch Instruments Inc, Burlington, MA 01803, United States

GRAPHICAL ABSTRACT

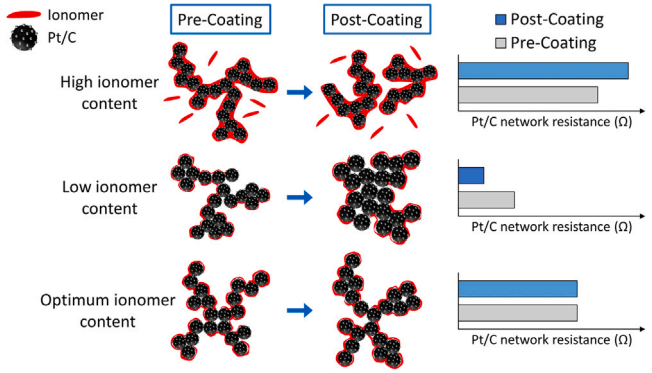

ARTICLE INFO

Keywords:
Catalyst ink
Rheology
Impedance
Microstructure
Ionomer distribution
Mass transport

ABSTRACT

The performance of a proton exchange membrane fuel cell is highly dependent on the microstructure of the catalyst layer. The catalyst layer consists of a network of platinum supported by carbon particles mixed with an ion-conductive ionomer. Optimum coverage of ionomer on catalyst is essential in providing proton conductive pathways while maintaining minimal oxygen transport resistance. Considering that most of the catalyst and ionomer interactions occur as a result of ink formulation and evolution during the high-shear coating process, a new methodology involving a combination of ink flow properties and electrochemical impedance spectroscopy is introduced to study interparticle interactions in catalyst ink. Five ink samples with ionomer-to-carbon ratios ranging from 0 to 1 are used to investigate the interplay between ionomer and catalyst. The flow and impedance properties of the ink are measured simultaneously to investigate the agglomerate characteristics and the percolation of conductive catalyst in the catalyst ink, while fixing the carbon to solvent ratio. This study successfully demonstrate the effectiveness of the newly developed characterization tools, which can be used for evaluating new materials and processing parameters. The insights gained from this study can be applied to optimize the triple-phase-boundaries and form efficient electrode structure with low Pt loading to enhance overall fuel cell performance.

* Corresponding author at: Environmental Systems Graduate Group, University of California, Merced, CA 95343, United States.
E-mail address: abel.chuang@ucmerced.edu (P.-Y.A. Chuang).

https://doi.org/10.1016/j.apenergy.2024.122680
Received 7 June 2023; Received in revised form 17 December 2023; Accepted 15 January 2024
Available online 23 January 2024
0306-2619/© 2024 The Author(s). Published by Elsevier Ltd. This is an open access article under the CC BY-NC license (http://creativecommons.org/licenses/by-nc/4.0/).

1. Introduction

The intricate and uncertain nature of crude oil price dynamics emphasizes the imperative to explore renewable energy sources as more stable and sustainable alternatives. This approach can help mitigate economic and policy uncertainties associated with the volatile crude oil market [1]. Proton exchange membrane fuel cells (PEMFCs) emerge as highly promising and environmentally friendly renewable energy technology, providing high efficiency and zero emissions for power generation. Within a PEMFC, the electrodes play a crucial role, serving as the sites for electrochemical reactions that generate electricity, producing water and heat as byproducts. The microstructure of these electrodes comprises porous catalyst agglomerates mixed with and covered by ion-conductive ionomer [2].

The catalyst typically consists of platinum nanoparticles, ranging in size of 2–5 nm, distributed either on the surface or within nanopores of various solid and mesoporous carbon supports. Given the sluggish nature of the oxygen reduction reaction (ORR), the cathode catalyst layer generally contains a higher loading of Pt to maintain reasonable fuel cell performance [3]. However, the high cost of Pt poses a significant barrier to fuel cell commercialization [4–6]. Consequently, reducing Pt loading by tuning the microstructure of the catalyst layer for enhanced Pt utilization at a lower loading is critically important. Electrochemical reactions can only take place at specific locations on the catalyst surface where all three pathways of mass, proton (H^+), and electron transport are available. These specific sites on the catalyst, known as triple phase boundaries (TPBs), are electrochemically active. Therefore, engineering the electrode to increase the number of TPBs becomes essential for improving fuel cell performance [7].

The catalyst layer in a PEMFC is typically fabricated through an ink coating method, involving the application of a suspension containing ionomer and catalyst agglomerates. This coating process is applied either directly onto a polymeric membrane or a decal substrate. The resulting three-layer structure, featuring anode and cathode catalyst layers on both sides of the membrane, is known as the membrane electrode assembly (MEA). This assembly is a pivotal component that significantly influences the performance and durability of a PEMFC. The microstructure of the catalyst layer is primarily shaped by the intricate interplay among its constituents in the precursor ink, a process greatly influenced by ink formulation. Berlinger et al. [8] extensively explored the correlation between catalyst ink components and parameters of the catalyst layer. Their results show that the formulation parameters of the ink, such as solvent composition, solid content, and ionomer-to-carbon ratio, emerge as critical contributors to the interactions within the ink, when considering constant ionomer and catalyst materials. These interactions involve ionomer-solvent, ionomer-catalyst/support, and catalyst-solvent interactions. Consequently, tailoring the structure of the catalyst layer necessitates a comprehensive understanding of these interactions among all its constituent materials [9–11]. The commonly employed solvents in catalyst ink formulation include water, isopropyl alcohol, and n-propanol (NPA) [8,12,13]. The choice of solvent formulation and solid content significantly affects properties such as catalyst agglomerate size, network formation, and ionomer conformation [14–19].

The ionomer-catalyst interaction is one of the most complex interactions in the ink, which directly affects the electrochemical and mass transport properties of the catalyst layer. The ionomer coverage on Pt/C must be adequate to provide proton transport to the catalyst sites while minimizing oxygen transport resistance towards the catalyst surface. In recent studies, a nonuniform ionomer coverage on the catalyst with thickness variation in the range of 4–10 nm and the co-existence of rod-like free ionomer aggregates (diameter 3 nm and length 20 nm) mixed with Pt/C agglomerates have been reported [10,20–23]. In this regard, some studies reported an ionomer loading in the range of 30–36 wt% as an optimum amount to achieve high proton conductivity in the catalyst layer [24]. However, this optimum amount of ionomer can vary depending on various parameters, such as catalyst and ionomer materials, catalyst loading, and test conditions [25]. Additionally, ionomer interaction with the carbon support occurs via van der Waals forces, while it is much more strongly adsorbed on the platinum surface [26]. The multi-level interactions in the catalyst ink make it difficult to establish property-performance correlations from in-situ fuel cell performance or ex-situ microscopy. Therefore, a technique that can evaluate bulk responses of the catalyst ink microstructure as a function of formulation variables is required.

Recently, several studies have employed rheology as a tool to examine the bulk properties of carbon-based suspensions, which serve as precursors for components in the catalyst layer [19,27–31]. Carbon networks with varying degrees of percolation can form due to ink formulation and evolution during processing. Consequently, the ink's resistance to flow can serve as an indicator of agglomerate structure, offering insights into the final microstructure of the catalyst layer, as observed in Cryo-SEM images reported by Takahashi et al. [22]. Catalyst ink, like most agglomerated carbon suspensions, has been found to exhibit shear thinning behavior [27,32]. While the flow resistance of the catalyst ink provides valuable information about its bulk properties, it lacks insights into ionomer-Pt/C interaction. Additionally, the carbon-to-solvent (C/S) ratio emerges as the primary contributor to catalyst ink viscosity [19,30]. Notably, a study of the ionomer-to-carbon (I/C) ratio in a PEMFC catalyst ink may be confounded by varying the C/S ratio, an aspect not consistently addressed in the literature. Therefore, this study proposes a systematic approach to investigate the catalyst ink with a constant C/S ratio across various ionomer contents. This work provides crucial information for designing electrodes for practical fuel cell applications, as I/C is a crucial design parameter for achieving high-performance electrodes in PEMFCs. Given that ionomer is an ion-conductive polymer and the catalyst network is electrically conductive, the electrochemical properties of the catalyst ink, such as its alternating current (AC) impedance, can serve as a complementary tool to rheology measurements. Narayanan et al. [33] explored the influence of shear on the rheological and electrical impedance behavior of Ketjen black (KB) suspensions in a solid-state flow battery (SSFB) solvent. The findings highlight the impact of altering shear rates on the agglomerate structure of KB, suggesting potential benefits for SSFBs, including reduced electronic resistance and improved yield stress under specific shear conditions. These findings may also apply to systems using fractal carbon blacks, such as flow supercapacitors. In another rheo-impedance-based study, Narayanan et al. [34] found that cycling in an LTO-based SSFB anolyte results in increased electronic resistance during lithiation and decreased yield stress, primarily due to the formation of an solid-electrolyte interphase (SEI) layer. This emphasizes the importance of SEI-free chemistry in SSFB development. Brilloni et al. [35] investigated the impact of ion concentration in super-concentrated electrolytes on the electronic percolating network of carbonaceous slurries. The findings suggest that super-concentrated electrolytes not only provide high electrochemical stability but also enhance the stability and electronic conductivity of the slurry. These insights may contribute to understanding and predicting the structural and rheological responses of catalyst layers in PEMFCs when engineered with specific polymer properties and processing conditions.

Motivated by the insights gained from Rheo-Impedance studies of flow batteries [33–36], we are conducting a comprehensive investigation using combined electrochemical impedance spectroscopy (EIS) and rheological measurements for the catalyst ink in PEMFCs. This approach aims to unravel the ionomer coverage and its interaction with the catalyst concerning network impedance. To facilitate impedance measurements, the rheometer has been adapted, allowing for an in-house Rheo-Impedance setup. The impedance of catalyst inks with varying ionomer contents is assessed both before and after exposure to high-shear conditions, mimicking the coating process. The results obtained from Rheo-EIS measurements are compared and validated

by cryo-TEM images capturing ionomer-covered catalyst agglomerates. Ultimately, the microstructural insights into the ink and catalyst layer contribute to understanding the performance of the fabricated Membrane Electrode Assembly (MEA) through fuel cell experiments. This study introduces a novel tool for investigating and quantifying ionomer-catalyst interactions, a pivotal factor in optimizing electrodes for high catalyst utilization, low platinum loading, and exceptional fuel cell performance.

2. Experimental

2.1. Sample preparation

The desired amount of 40 wt% Pt/C (Johnson Matthey, HiSPEC 4000) catalyst powder and ionomer dispersion (D2020, Ion Power Inc.) were mixed in a water-IPA solvent (IPA/Water = 0.30) to prepare the catalyst inks. The carbon to solvent (C/S) ratio was fixed at 0.06 for all studied inks to eliminate the varying effect of solvent-carbon interaction and focus on the study of the ionomer-carbon-catalyst interactions. Five levels of ionomer content, I/C = 0, 0.25, 0.50, 0.75, and 1, were designed to investigate the interparticle interactions. The ionomer dispersion and solvents were mixed in a vial using a sonication bath and then added to the catalyst powder in a plastic jar with eight Zirconia beads of 5 mm diameter. Liquid and solid components were mixed via centrifugal ball milling inside a Thinky mixer at 2000 rpm for 3 min. Although the samples of I/C = 0 and 0.25 are not practical for fuel cell applications, they were studied to understand the role of ionomer in the microstructure formation of the catalyst ink and the catalyst layer. Only the catalyst inks with I/C = 0.50, 0.75, and 1 were evaluated through fuel cell performance. The catalyst ink was coated on a virgin PTFE substrate with the desired loading and then air-dried. The catalyst layer was then transferred to a 25 μm Nafion NR211 membrane (Ion Power, Inc.) via a hot-press process under the conditions of 132 °C and 300 psi for 5 min.

2.2. Rheology and rheo-impedance

Rheological measurements were conducted using a Rheometer from NETZSCH Instrument with standard roughened parallel plate geometries (40 mm diameter). The instrument was modified with in-house geometries for simultaneous rheological and EIS measurements. The schematic diagram of the resulting setup is illustrated in Fig. 1 and the setup with a loaded sample is shown in Figure S1. The upper and lower geometries (40 mm diameter) were machined from a 304 stainless steel rod followed by surface sandblasting to provide surface roughness that prevents particle slipping during the application of high shear rate. The upper plate rotates while the lower plate remains stationary. A Teflon adaptor was used to electrically isolate the upper plate from the rheometer body, however, the challenge was to ensure that a good alignment between the geometries was achieved. To maintain an electrical connection to the upper geometry with minimum friction, a liquid metal (Gallium Indium Eutectic, EGAIN, Sigma Aldrich) [37] was used in the solvent trap connected to the upper geometry. A stainless steel needle was immersed in the solvent trap and connected to the potentiostat (CH Instrument 750E). Further calibration results indicate that the in-house setup provides a suitable electrical connection and has low friction, thereby not interfering with the applied torque from the rheometer. The lower stainless steel plate was attached to a Peek geometry (NETZSCH Instrument) for electrical insulation. Therefore, the two metallic upper and lower plates act as two electrodes with the catalyst ink as the media to be studied between them.

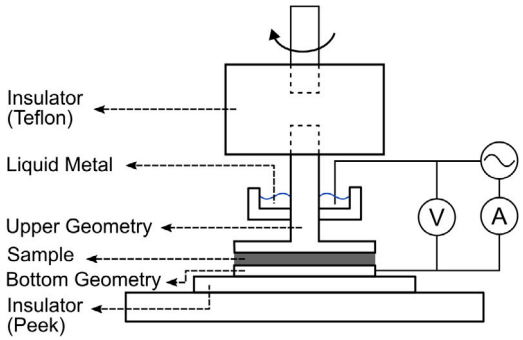

Fig. 1. Schematics of the Rheo-Impedance setup consisted of two metallic geometries, one solvent trap containing liquid metal and two electrical insulation from the upper and lower body of the Rheometer.

2.2.1. Rheo-impedance setup calibration

Due to the significant changes in the in-house setup compared to the standard geometries, it was necessary to ensure the mechanical stability and accuracy of the applied shear forces to the sample. To achieve this, a Newtonian standard calibration oil with a known viscosity (1 Pa.s) was tested in the modified setup for the desired range of shear rates. As shown in Figure S2, the setup was able to pass the standard oil calibration test with high accuracy. The working gap between the geometries was set to 0.30 mm, which is suitable for the catalyst ink characterizations [27]. It is well known that the impedance increases with increasing electrode distance (in this case, the geometry gap) [38]. To rule out the effect of the working gap on sample impedance, EIS measurements were performed on a catalyst ink sample in the stationary mode at gaps of 0.25, 0.30, 0.40, and 0.50 mm and a voltage amplitude of 50 mV with a frequency range of 0.01–10^5 Hz. As observed from Figure S3 and S4, the impedance increases with the gap almost linearly. From the rheological perspective, a gap ten times higher than the largest particle in the sample is appropriate for the measurements [39]. Typically, the catalyst ink agglomerates are in the order of 1 μm [40], so a gap larger than 0.25 mm is appropriate for the measurements. Due to improved torque-related stability, a working gap of 0.30 mm was used for the rheo-EIS measurements in our study, which is large enough for the rheological measurements and small enough to reduce the impedance induced by the electrode distance.

The AC perturbation voltage required for EIS measurements should be selected from the sample's linear range of the I-V curve [41]. Consequently, linear sweep voltammetry (LSV) was conducted in the range of −0.20~0.20 V at high (0.10 V/s) and low (0.01 V/s) scan rates. These measurements were performed with a catalyst ink sample loaded in the Rheo-EIS geometry and in the stationary mode. Based on the results shown in Figure S5, 50 mV was chosen as the AC perturbation voltage for all EIS measurements.

2.2.2. Rheo-impedance parameters to evaluate catalyst ink microstructure

Two sets of Rheo-Impedance experiments were performed: (a) simultaneous three-phase rebuilt and a single frequency EIS measurement and (b) full range EIS measurement before and after a high shear force resembling the coating/processing condition. Prior to any rheological test, the ink was pre-sheared at 1 s^{-1} and rested for 2 min to remove any prior shear history and provide all samples with a similar starting point. For the three-phase rebuilt measurement, the sample was held at a shear rate of 0.1 s^{-1} for 200 s to provide pre-coating (storage) conditions for the ink. Then, the shear rate was ramped up to 1000 s^{-1}, simulating high shear coating conditions for the ink, and held for 200 s. Finally, the shear rate was reduced back down to 0.1 s^{-1} to simulate the post-coating recovering condition as a thin film. To allow the microstructure to fully recover, measurements were taken at this condition for 720 s. Parallel to all three-phase rheological

measurements, a single frequency (0.50 Hz) impedance test at a voltage amplitude of 50 mV was carried out to measure the impedance of the sample under dynamic shearing conditions. A dwelling time of 200 s was used after applying high shear rates to ensure the required stability for EIS measurements.

In the second set of the experiments, a full frequency range (f = 0.01~10^5 Hz) EIS measurement was performed on the inks before and after applying a high shear rate (1000^{-1} for 200 s) to capture the true resistance of the Pt/C network in stationary. The equivalent circuit as shown in Figure S6 was used to fit the EIS data. This equivalent circuit represents a parallel electrical resistance (R_1) and ionic resistance (R_2) provided by the carbon support agglomerate network with dissolved ions such as H^+ in the solution, respectively. The constant phase element (CPE,Q) is due to the capacitor effect of ion accumulation on the electrode (geometry) surface. The intermediate frequency region of the EIS impedance showed a curve depression (45° region), indicating some properties of charge diffusion resistance on the electrode surface that could be fitted using a Warburg (w) element. However, this Warburg effect has minimal impact on the overall impedance of the ink and requires advanced modeling [42] that is beyond the scope of this work. In general, it is expected that effect of I/C ratio and all interparticle interactions are reflected in the microstructure of the Pt/C particles, which can be studied through the electrical resistance of the catalyst ink.

2.3. Cryogenic transmission electron microscopy

The Catalyst ink samples with I/C ratios of 1 and 0.50 were diluted with IPA to achieve transparent vitreous ice. Ink dilution with IPA may break down the large agglomerates but does not affect the primary aggregates due to their strong bonding [43]. The sample preparation was performed in Vitrobot. Three μL of the suspension was deposited on a carbon-coated copper grid (300 mesh, Tedpella) and turned into vitreous ice using liquid ethane in Vitrobot. The sample was stored in liquid nitrogen and transported to the TEM, Talos F200C G2, for imaging at an operating voltage of 200 kV.

2.4. In-situ fuel cell characterizations

Fuel cell experiments were performed on the MEAs with I/C = 0.50, 0.75, and 1. Toray TGP-H-060 with 5 wt% PTFE impregnation and a microporous layer were used on both the anode and cathode sides as gas diffusion media. A straight parallel flow field was used with a cell active area of 2 cm^2 in an automated Greenlight G20 fuel cell test station. To evaluate the ohmic resistance in the cell, high-frequency resistance (HFR) of the cell was measured via EIS using Gamry Reference 3000 coupled with a Gamry 30k Booster.

Cyclic voltammetry (CV) was performed under H_2/N_2 environment at a scan rate of 50 mV/s to measure the electrochemically active surface area (ECSA) of the electrode. After the cell was pre-conditioned, a series of fuel cell performance testing protocols were performed (Table S1). Dry limiting current tests were performed at 80 °C, 64% RH, and 100~300 kPaa. Oxygen dry mole fraction was varied between 1 and 4%. Fuel cell performance was evaluated through potentiostatic load control of 6 min under each potential at 70 °C, 60% RH, and 100 kPaa. The relative humidity (RH) sweep test was performed by sweeping the RH from 20 to 100%, maintaining each RH condition for 20 min, and averaging the last minute of current density at a voltage of 0.30 V. Proton transport resistances in the membrane and cathode catalyst layer was also evaluated through EIS measurements under H_2/N_2 environment at 70% RH.

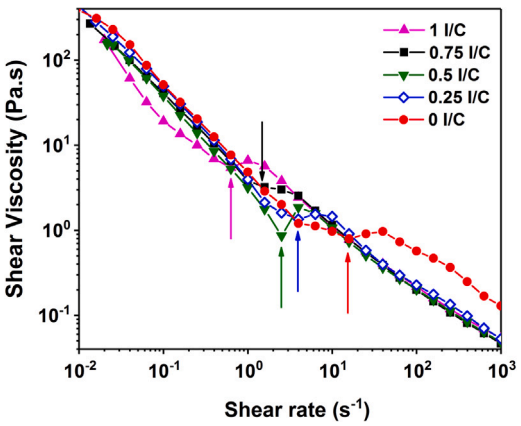

Fig. 2. Shear viscosity as a function of shear rate of the catalyst inks with I/C = 0, 0.25, 0.5, 0.75, and 1.

3. Results and discussion

3.1. Catalyst ink viscosity

The viscosity of the catalyst ink reveals its microstructure-driven flow resistance as a function of the applied shear force. In addition to the microstructural information, the ink viscosity at high shear rates (>500 s^{-1}), which resembles the realistic coating process, can be extracted from a flow curve. The flow curve of catalyst inks with constant carbon/solvent ratio and various ionomer/carbon ratios is shown in Fig. 2. The samples exhibit typical shear thinning behavior of carbon-based ink, with transient shear thickening at intermediate shear rates. Due to the same carbon to solvent ratio, most samples exhibit similar viscosity at low shear rates (<0.1 s^{-1}), except for the I/C = 1, which has the highest ionomer content. The shear thinning index, which is an indication of the extent of shear thinning behavior of the suspension, is extracted from a power law fit to the viscosity curve [19,44]. For all samples, the viscosity at low shear and the shear thinning index are summarized in Table 1. The sample with I/C = 1 has the lowest shear thinning index, indicating a faster agglomerate breakdown. At low shear rates, shear thinning is due to the breakdown of large agglomerates connected by weak van der Waals forces. Thus, the Pt/C agglomerates in the sample with I/C = 1 might have weaker bonding due to thicker ionomer coverage. The rise in viscosity at intermediate shear rates results from the dominance of hydrodynamic forces and transient particle growth [19]. The onset of this transient behavior is shown by arrows in Fig. 2, and it is shifted towards lower shear rates with increasing I/C ratio, which implies a potentially higher particle volume for the inks with higher I/C ratio and as a result formation of transient agglomerates at lower shear forces [35,45]. Finally, at high shear rates, where agglomerates are potentially broken down into primary aggregates, the sample with I/C = 0 ended up having the highest viscosity. This indicates that pure carbon–carbon interaction in the absence of the ionomer is much stronger. Therefore, adding ionomer seems to weaken carbon–carbon interactions, resulting in a less percolated carbon network.

3.2. Rheo-impedance measurement under transient conditions

Preparation of the catalyst layer from its precursor ink typically can be mimicked by three steps of applied shear forces: (1) the ink is kept in storage under low shear/stationary conditions, (2) the ink undergoes a high shear coating process, and (3) the ink returns to the low shear/stationary condition during post-coating recovery. To evaluate catalyst ink's microstructural evolution in forming a thin film, three steps of low-high-low shear rates were applied to the catalyst ink

Table 1
Low shear viscosity and shear thinning index of catalyst inks with various Ionomer/Carbon ratios. The reported values are calculated from shear rates of 0.01–0.1 s^{-1}.

I/C ratio	Low shear viscosity at 0.1 s^{-1} (Pa s)	Shear thinning index (shear rate < 0.1 s^{-1})
0.00	51.41	0.126
0.25	49.55	0.078
0.50	37.95	0.053
0.75	40.78	0.056
1.00	19.16	−0.378

along with electrochemical impedance measurements. Fig. 3(a) shows viscosity as a function of time under the three-step shear conditions, while Fig. 3(b) provides impedance information of the corresponding sample with a small AC perturbation at the frequency of 0.5 Hz. In the first step under low shear, the viscosity of all samples is relatively close, as expected from the flow curves as shown in Fig. 2. However, the sample impedance increases with increasing I/C ratio due to either ionomer coverage around agglomerates or the presence of free ionomer in the ink [46]. By switching to high shear rate in the second step, the viscosity drops sharply due to agglomerate breakdown and re-aligning with the shear flow direction. As a result, the impedance increases as shown in Fig. 3(b) at t = 200 s due to the sudden interruption in the conductive paths [33]. This impedance rise remains constant or slightly decreases over time for samples with I/C = 1 and 0.75. On the other hand, the impedance diminishes more sharply under high shear for samples with I/C < 0.75. During the second step, the inter-particle distance decreases by breaking down more agglomerates and increasing the total particle volume over time, which results in lower impedance. This reduction in impedance at high shear rate is less significant for samples with high ionomer content (I/C = 1 and 0.75) indicating the existence of more ionomer coverage around carbon aggregates, which disrupts electrical conductivity.

During the third step, when the shear rate is reduced rapidly back to the initial value, the samples with I/C < 0.75 experience an overshoot in the viscosity, indicating more elastic behavior due to faster aggregation kinetics and low inter-particle repulsive forces [47]. In contrast, the samples with I/C ≥0.75 demonstrate a damping behavior in response to the particle collision, which is likely due to higher repulsive forces from ionomer coverage. Over time, the viscosity overshoot is diminished as the particles interpenetrate and stabilized. To evaluate the microstructure transformation in response to high shear force, the viscosity in the third stage is normalized by the average viscosity in the first stage as shown in (Figure S7). Results show that samples with higher ionomer content are unable to recover back to their original microstructure due to lower particle interaction. The samples with lower ionomer content not only fully recover the microstructure, but also build an even stronger one, as seen in the extreme case of I/C = 0. These results suggest that increasing the ink's ionomer content hinders carbon–carbon attraction due to the repulsive force from ionomer coverage, resulting in a less dense microstructure after experiencing high shear rate. This explains the minimal change in the impedance for samples with I/C = 0.75 and 1 at the first and third step. Conversely, samples with lower ionomer content benefit from carbon–carbon attraction, and after breaking down into smaller aggregates at high shear rates, particles could build a denser network resulting in lower impedance, as shown in Fig. 3(b).

3.3. Stationary impedance measurement of catalyst inks before and after high shear rate

To fully understand the suspension's ionic and electrical resistance, a full range frequency EIS measurement was conducted on the stationary samples before and after subjecting the ink to high shear rate. The Nyquist plot of the impedance data of all five samples are shown in

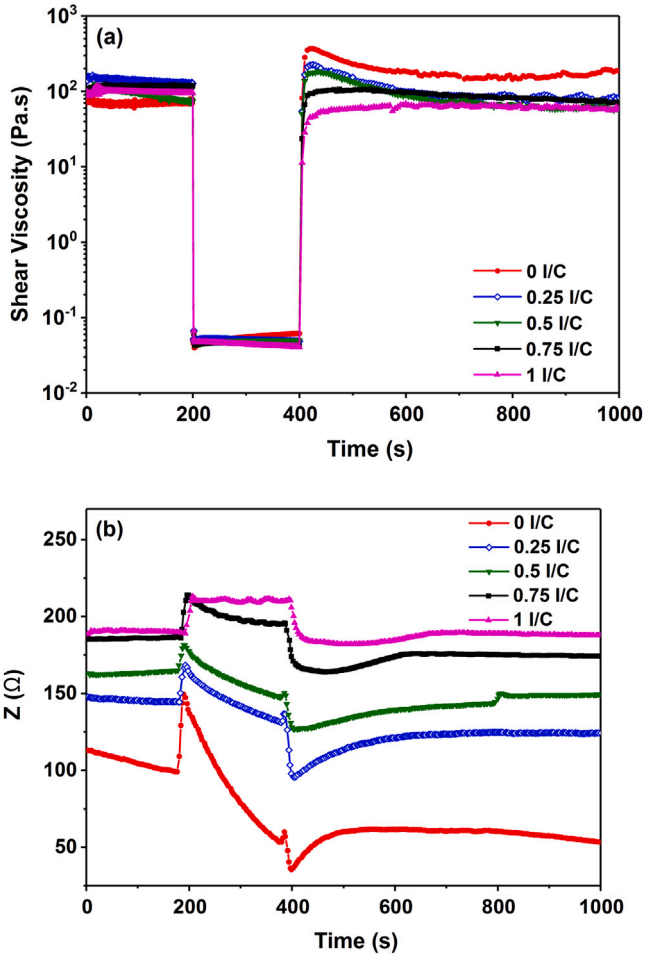

Fig. 3. Simultaneous three phase rebuilt analysis of catalyst inks: (a) viscosity measurement and (b) impedance results at 0.5 Hz. Three steps of the applied shear rate are (i) 0.1 s^{-1} for 200 s, (ii) 1000 s^{-1} for 200 s, and (iii) 0.1 s^{-1} for 720 s.

Fig. 4. The radius of the semicircle represents the sample impedance, which is the smallest when there is no ionomer present (I/C = 0). An equivalent circuit presented in S6 was used to fit the EIS data. At high frequencies, the EIS intercept with the *x*-axis represents the parallel ionic and electrical resistances of the ink, while the low-frequency impedance represents mostly the electrical resistance of the conductive carbon network in the ink. The electrical resistance in the equivalent circuit was found to be the major contributor to the impedance of the catalyst inks. The electrical resistances as a function of I/C ratio before and after shear is summarized in Fig. 5. Before shear, the resistivity increases almost linearly up to I/C = 0.75 and then reaches a plateau at I/C = 1.0. This suggests that the agglomerated network weakens resulting in a less conductive and loose gel microstructure due to the increasing ionomer content. At the critical I/C of 0.75, the thickness or coverage of the ionomer around Pt/C is significant enough that adding more ionomer does not significantly affect the microstructure.

Comparing with before-shear data, samples with I/C < 0.75 show a significantly decreased resistance after applying a high shear force. The resistance remained the same for I/C = 0.75 and slightly increased for I/C = 1, which is consistent with the observations in the first and third steps in three-phase rebuild testing. This finding suggests that I/C = 0.75 is the highest value at which Pt/C could still build up a well-percolated cohesive network. Adding more ionomer than I/C = 0.75, the ionomer coverage could induce a repulsive force between particles and hinder the formation of compact interconnected agglomerates, resulting in a less dense and locally less conductive microstructure.

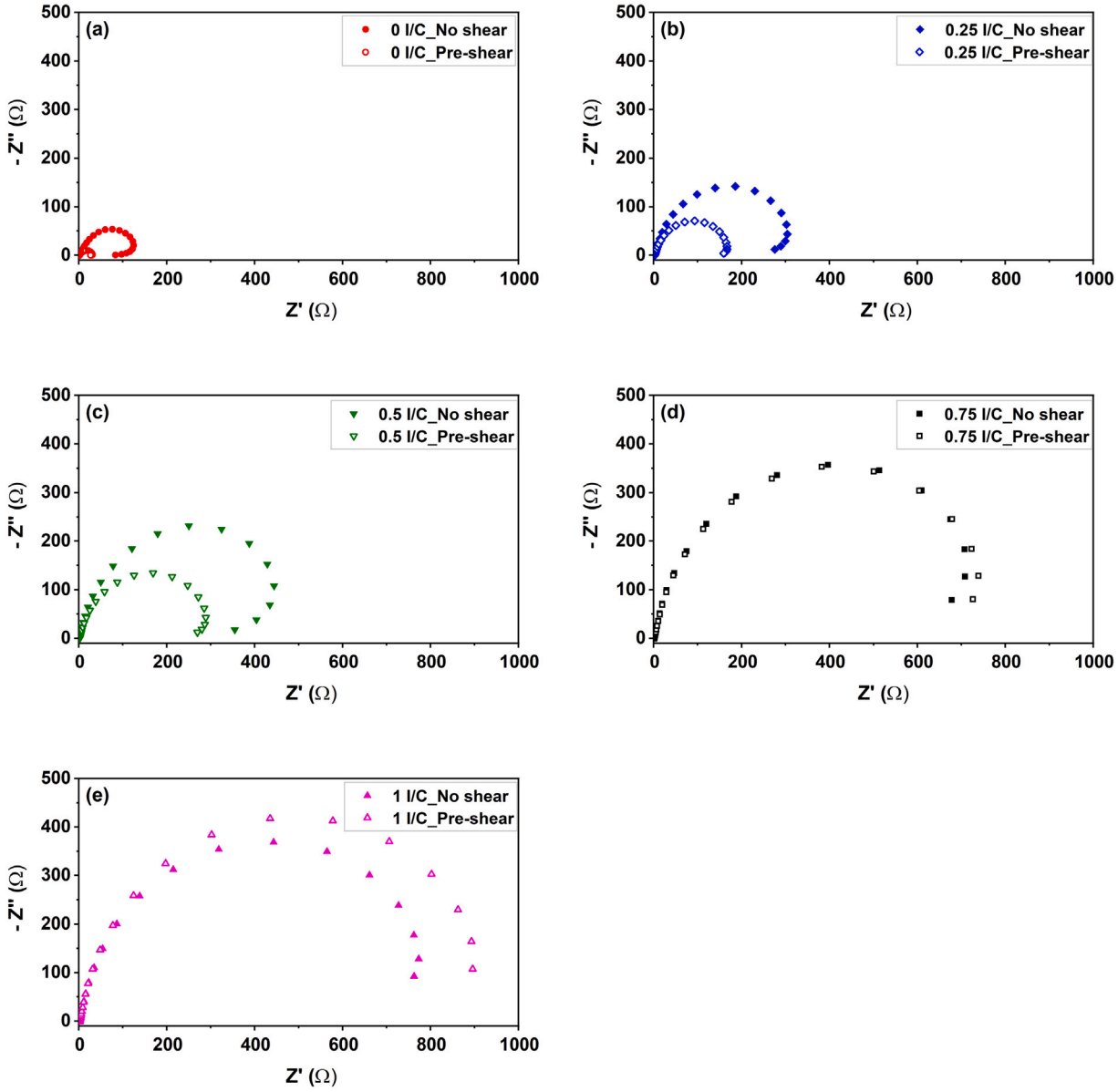

Fig. 4. Full range (f = 0.01–10^5 Hz) EIS measurement of the catalyst inks in the Rheo-EIS setup before and after applying a shear rate of 1000 s^{-1} for 200 s.

Further, it is expected that the sample with I/C = 1 contains free ionomer aggregates that could contribute to the overall high network resistance of the catalyst ink [46].

3.4. Electrochemical impedance and rheology of pure carbon ink

Equivalent carbon inks without platinum were prepared to further deconvolute the inter-particle interactions in the catalyst ink. Nano platinum particles have a tendency to interact closely with the ionomer [27,48,49], which consumes a significant portion of the ionomer through Pt-ionomer bonding. A similar recipe of the catalyst ink was used to prepare pure carbon (Vulcan XC-72) ink without platinum. During the rheological measurement, the pure carbon ink shows a drastic decrease in viscosity, indicating that a significant amount of ionomer interacts with Pt, which is not present in pure carbon ink. Without platinum, the ionomer tends to cover all carbon particles and hinders the formation of interconnected microstructure, causing the sample to behave more like a Newtonian fluid at high shear rates as shown in Figure S8 [27]. The electrochemical impedance of the pure carbon ink with I/C = 1 before and after the high shear is

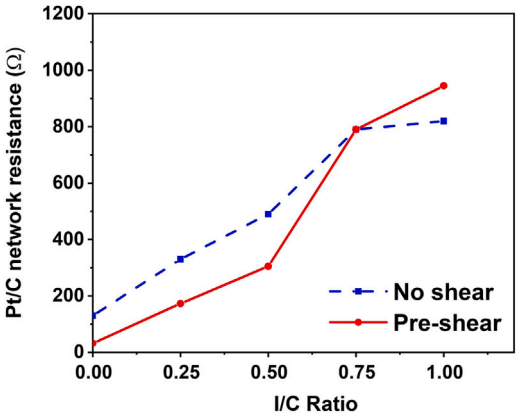

Fig. 5. Electrical resistance of the Pt/C ink network measured from the fitted equivalent circuit of the EIS measurement from Fig. 4.

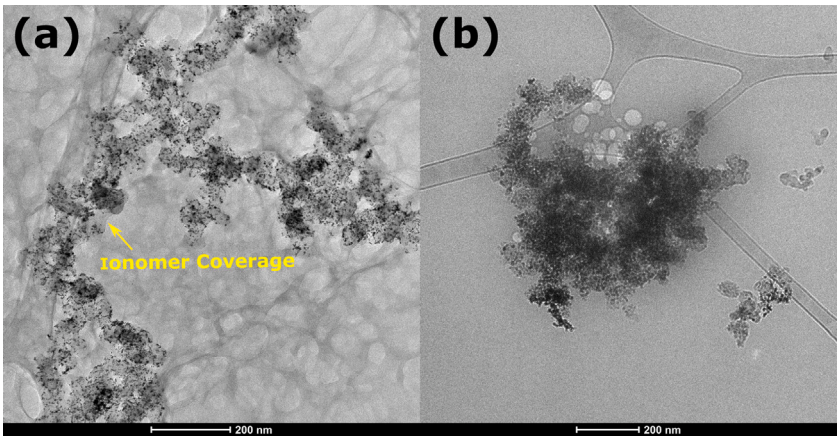

Fig. 6. Cryo-TEM images of the diluted catalyst inks with (a) I/C = 1 and (b) I/C = 0.5.

shown in Figure S9. The lack of a conductive carbon network results in an extremely high electrical resistance. Although the Nyquist plot [45] did not show a semicircle, the data was successfully fitted using the equivalent circuit similar to that used for the catalyst ink sample. It was found that the electrical resistance was more than one order of magnitude higher than that of the corresponding catalyst ink. The results indicate that the ionomer interacts much more strongly with Pt compared to carbon nanoparticles. Even though the methods developed in this study can be applied to study catalyst ink, the specific results obtained cannot be directly applied to catalyst ink made from Pt-free catalysts.

3.5. Cryogenic transmission electron microscopy of the catalyst aggregates

To study the microstructure of the aggregates in the ink, the catalyst ink was diluted with IPA to create more transparent vitreous ice for cryo-imaging. The catalyst inks with I/C = 0.5 and 1 were selected as suitable lower and upper limits for a functional catalyst layer in a fuel cell. From Fig. 6(a), it is evident that the sample with I/C = 1 has an open fractal shape aggregate with a thick layer of ionomer coverage as marked on the figure. The rheological and impedance measurements of I/C = 1 suggest a loose structure, which agrees with the expanded shape of the primary aggregates observed from the TEM image. On the other hand, the primary aggregates of the sample with I/C = 0.5 are more spherical and compact as shown in Fig. 6(b). This compact shape is resulted from the high carbon–carbon interactions indicated by the low resistance and high microstructural strength observed from the Rheo-EIS results. Additional cryo-TEM images of the studied samples with I/C = 0.5 and 1 can be found in Figure S10.

3.6. Characterization and performance of the catalyst layer

3.6.1. Oxygen transport resistance

Limiting current measurements were used to evaluate the oxygen transport resistance (OTR) in different components of a fuel cell [50]. The limiting current experiments were conducted under relatively dry RH conditions in a differential cell to obtain oxygen transport resistance in the GDM and catalyst layer in the absence of liquid water. As shown in Figure S11, the slope of transport resistance versus pressure plot represents the Fickian or pressure-dependent diffusion that occurs in the large pores of the porous media, while the intercept represents pressure-independent transport resistance from Knudsen or thin film diffusion. Since the same Toray-TGP-H-060 GDM was used for all fuel cell testing, the Fickian diffusion, which can be represented by the ratio of nominal diffusivity and the effective diffusivity or D/D_{eff}, is about the same for all samples as shown in Table 2. Any change in the intercept or R_{Others} between these three samples can be mostly attributed to the difference in the catalyst layer, as the microporous layer of the GDM remains the same. As observed from Table 2, the catalyst layers with I/C = 0.5 and 0.75 yield similar R_{Others}, whereas the catalyst layer with I/C = 1 shows around 25% increase in R_{Others}. The increased ionomer coverage or thicker film of I/C = 1 would induce higher transport resistance and reduce the oxgyen concentration on the Pt surface [46,51,52]. Similar observations were also made by Wen et al. where they used low Pt loading catalysts on the cathode side and obtained an increasing trend of pressure-independent oxygen transport resistance for higher I/C ratios (ranging between 0.40 to 1.2) because of the thicker ionomer layer covering the catalyst surface. [53]. Schneider et al. also used the oxygen limiting current technique for Pt catalyst MEAs and claimed that the diffusion resistance increases with high I/C ratios (ranging between 0.50 to 1.2) due to pore blocking and the addition of more ionomers to the Pt [54]. The limiting current results validate our observations from the rheo-impedance results and cryo-TEM images.

Table 2
The oxygen transport resistance measured from dry limiting current experiments.

Cathode I/C	D/D_{eff}	R_{Others} (s/cm)
0.50	3.30	0.249
0.75	3.23	0.248
1	3.09	0.310

3.6.2. Fuel cell performance characterization

Hydrogen adsorption and desorption method is used to measure the electrochemically active surface area (ECSA) of the catalyst layer. The ECSAs measured at 100% RH were 15.58, 17.55, and 19.46 m^2_{Pt}/g_{Pt} for the catalyst layers with I/C = 0.5, 0.75, and 1, respectively. The increase in the ECSA with increasing ionomer content can be attributed to the increasing proton conductive pathways due to high ionomer coverage [55].

The proton transport resistances in the catalyst layers and the membrane are evaluated by electrochemical impedance spectroscopy under 100% RH with H_2/N_2 flow at the anode/cathode, respectively [56]. The proton resistances for all three samples are tabulated in Table 3. It is observed that the proton resistance in the cathode increases with decreasing I/C ratio. The sample with I/C = 0.5 shows the highest proton transport resistance, likely due to insufficient ionomer coverage or connectivity on the catalyst. Conversely, the sample with I/C = 1 exhibits the lowest proton transport resistance, followed by the sample with I/C = 0.75. This trend is similar to as observed by Wen et al. and Yakovlev et al. where they claimed the development of improved proton conducting domains with increased I/C ratios [53,57].

The fuel cell performance was evaluated via an *i*-V polarization curve, as shown in Fig. 7(a). The voltage losses with the increase in

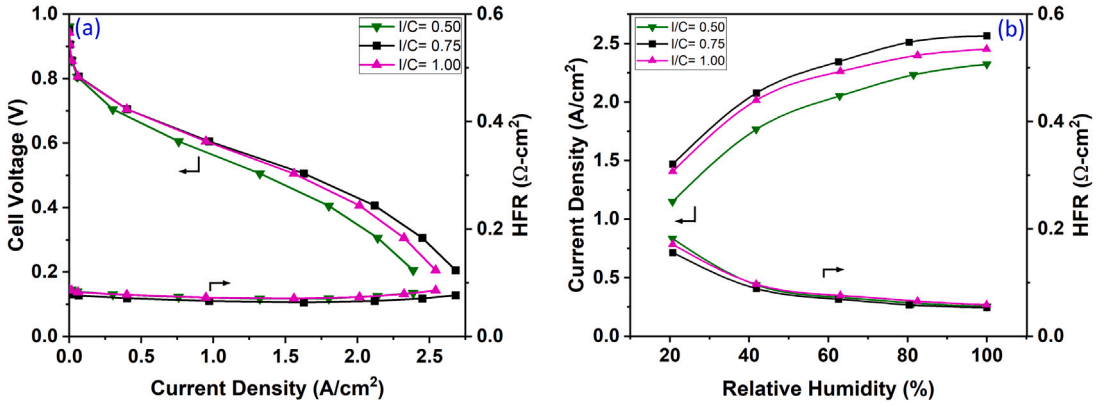

Fig. 7. (a) Steady-state polarization curve at 70 °C, 60% RH, and 100 kPa., and (b) current density and HFR as a function of relative humidity at 70 °C, 20~100% RH, 100 kPa., 0.30 V potentiostatic hold.

Table 3
Proton transport resistance in the cathode catalyst layer and membrane at 70 °C, 70% RH, 300 kPa abs., 0.20 V DC with 10 mV AC perturbation.

Cathode I/C	Cathode proton resistance (mΩ-cm^2)	Membrane proton resistance (mΩ-cm^2)
0.50	109.23	53.68
0.75	42.63	48.79
1	31.62	53.10

current density are attributed to kinetic, ohmic, and mass transport losses, respectively. The kinetic voltage losses under low current densities are similar for all samples. The membrane resistance measured by high frequency resistance (HFR) are also similar. However, the sample with I/C = 0.50 shows lower performance in the linear ohmic region, which is likely due to less effective proton conductive pathways in the cathode catalyst layer as shown in Table 3. Overall, the sample with I/C = 0.75 shows the best performance followed by I/C = 1 and 0.50. The relatively lower mass transport performance at high current density for the sample with I/C = 1 agrees well with its high oxygen transport resistance measured from the limiting current experiment as shown in S11. We also performed relative humidity (RH) sweep at a voltage of 0.30 V to evaluate the performance as a function of RH as shown in 7(b). It can be observed that the performance increases with increasing RH mostly due to the decrease of the membrane resistance. For the three samples studied, the overall performance align closely with that in the polarization performance that I/C = 0.75 performs the best followed by I/C = 1 and 0.50. In conclusion, the sample with I/C = 0.75 exhibits a relatively lower, yet sufficient, ionomer coverage for effective proton transport with adequate open pores for oxygen transport, making it the best candidate for achieving the optimum fuel cell performance. This critical I/C was successfully identified with the Rheo-EIS microstructural evaluation and validated by its superior fuel cell performance.

4. Conclusion

In this study, a novel approach is introduced to quantify the impact of ionomer content on Pt/C-ionomer interactions by leveraging the flow properties and network impedance of the fuel cell catalyst ink. The rheological flow curves exhibit consistent shear-thinning behavior across all samples. Notably, the sample without ionomer content displays the highest viscosity at high shear rates, indicating a robust percolated microstructure. In the absence of ionomer (I/C = 0), the post-shear microstructure is even more compact than the structure before shearing. In contrast, as the I/C ratio increases, the post-shear structure could not fully recover to its original viscosity, suggesting a looser carbon network with increasing ionomer content. The impedance of the ink significantly increases with the I/C ratio, indicating that thicker ionomer coverage induces repulsive forces among the carbon, leading to reduced carbon–carbon interaction. This phenomenon explains the lower post-shear recovery and the loose microstructure observed in three-step shear tests. For our baseline materials, the impedance spectra identify I/C = 0.75 as a crucial turning point, where values below this lead to decreased impedance as a result of high shear force and break down of the agglomerates to smaller pieces. On the other hand, network resistance increases in post-shear conditions for samples with I/C > 0.75, signaling a significant deterioration in carbon network connection at higher I/C ratios. Cryo-TEM imaging reveals more open and expanded primary aggregates for I/C = 1.0, in contrast to compact and spherical primary aggregates for I/C = 0.5. Cryo-TEM analyses also detect thick ionomer coverage for I/C = 1.

Lastly, catalyst layers are fabricated with I/C = 0.5, 0.75, and 1.0, and their fuel cell performance is evaluated. The sample with I/C = 1 exhibits higher oxygen transport resistance, while I/C = 0.75 shows resistances similar to I/C = 0.5. Further, I/C = 1 demonstrates increased mass transport loss in the i-v curve, while I/C = 0.75 offers superior performance. I/C = 0.5, with a higher proton resistance, performs less efficiently in the ohmic region. Remarkably, I/C = 0.75 shows slightly higher proton resistance at the cathode catalyst layer compared to I/C = 1, but it exhibits the least membrane resistance and, importantly, provides the best fuel cell performance across a broader range of relative humidity conditions. Therefore, the optimal I/C ratio is determined to be 0.75, offering proper ionomer coverage for low proton resistivity, sufficient carbon–carbon interaction for electron conduction, and reduced local oxygen transport resistance induced by ionomer thickness around the catalyst. The results of our study successfully demonstrate the effectiveness of the newly developed Rheo-Impedance tool for evaluating new materials and optimizing designs to advance fuel cell and electrolysis technologies.

CRediT authorship contribution statement

Shirin Mehrazi: Writing – original draft, Methodology, Formal analysis, Data curation, Conceptualization. **Taymaz Homayouni:** Writing – original draft, Methodology. **Nitul Kakati:** Writing – original draft, Investigation, Data curation. **Mrittunjoy Sarker:** Writing – original draft, Investigation, Formal analysis, Data curation. **Philip Rolfe:** Methodology, Investigation. **Po-Ya Abel Chuang:** Writing – review & editing, Supervision, Methodology, Funding acquisition, Formal analysis, Conceptualization.

Declaration of competing interest

The authors declare that they have no known competing financial interests or personal relationships that could have appeared to influence the work reported in this paper.

Data availability

Data will be made available upon request.

Acknowledgments

This work is supported by the University of California (United States), Merced, the CIPHER Program (IIID 2018-008) from the Commission on Higher Education – Philippine California Advanced Research Institutes (CHED-PCARI) of the Republic of the Philippines, and the Million Mile Fuel Cell Truck (M2FCT) consortium, funded by the Department of Energy (DoE), US, under contract No. DE-AC02-05CH11231.

Appendix A. Supplementary data

Supplementary material related to this article can be found online at https://doi.org/10.1016/j.apenergy.2024.122680.

References

[1] Karasu S, Altan A. Crude oil time series prediction model based on LSTM network with chaotic henry gas solubility optimization. Energy 2022;242:122964.
[2] Rahman MA, Sarker M, Mojica F, Chuang P-YA. A physics-based 1-D PEMFC model for simulating two-phase water transport in the electrode and gas diffusion media. Appl Energy 2022;316:119101.
[3] Banham D, Ye S. Current status and future development of catalyst materials and catalyst layers for proton exchange membrane fuel cells: an industrial perspective. ACS Energy Lett 2017;2(3):629–38.
[4] Papageorgopoulos D. Fuel cell R&D overview, DOE hydrogen and fuel cells program annual merit review and peer evaluation meeting. Technical report, U.S. Department of Energy; 2019.
[5] Yin C, Yang H, Liu Y, Wen X, Xie G, Wang R, Tang H. Numerical and experimental investigations on internal humidifying designs for proton exchange membrane fuel cell stack. Appl Energy 2023;348:121543.
[6] Sadeghi MA, Khan ZA, Agnaou M, Hu L, Litster S, Kongkanand A, Padgett E, Muller DA, Friscic T, Gostick J. Predicting pemfc performance from a volumetric image of catalyst layer structure using pore network modeling. Appl Energy 2024;353:122004.
[7] Wei P, Chang G, Fan R, Xu Y, Chen S. Investigation of output performance and temperature distribution uniformity of PEMFC based on Pt loading gradient design. Appl Energy 2023;352:121962.
[8] Berlinger SA, Garg S, Weber AZ. Multicomponent, multiphase interactions in fuel-cell inks. Curr Opin Electrochem 2021;29:100744.
[9] Huang J, Li Z, Zhang J. Review of characterization and modeling of polymer electrolyte fuel cell catalyst layer: The blessing and curse of ionomer. Front Energy 2017;11(3):334–64.
[10] Karan K. PEFC catalyst layer: Recent advances in materials, microstructural characterization, and modeling. Curr Opin Electrochem 2017;5(1):27–35.
[11] Zamel N. The catalyst layer and its dimensionality–A look into its ingredients and how to characterize their effects. J Power Sources 2016;309:141–59.
[12] Ngo TT, Yu TL, Lin H-L. Influence of the composition of isopropyl alcohol/water mixture solvents in catalyst ink solutions on proton exchange membrane fuel cell performance. J Power Sources 2013;225:293–303.
[13] Welch C, Labouriau A, Hjelm R, Orler B, Johnston C, Kim YS. Nafion in dilute solvent systems: dispersion or solution? ACS Macro Lett 2012;1(12):1403–7.
[14] Orfanidi A, Rheinländer PJ, Schulte N, Gasteiger HA. Ink solvent dependence of the ionomer distribution in the catalyst layer of a PEMFC. J Electrochem Soc 2018;165(14):F1254.
[15] Park J-H, Shin M-S, Park J-S. Effect of dispersing solvents for ionomers on the performance and durability of catalyst layers in proton exchange membrane fuel cells. Electrochim Acta 2021;391:138971.
[16] Lei C, Yang F, Macauley N, Spinetta M, Purdy G, Jankovic J, Cullen DA, More KL, Kim YS, Xu H. Impact of catalyst ink dispersing solvent on PEM fuel cell performance and durability. J Electrochem Soc 2021;168(4):044517.
[17] Huang D-C, Yu P-J, Liu F-J, Huang S-L, Hsueh K-L, Chen Y-C, Wu C-H, Chang W-C, Tsau F-H. Effect of dispersion solvent in catalyst ink on proton exchange membrane fuel cell performance. Int J Electrochem Sci 2011;6(7):2551–65.
[18] Balu R, Choudhury NR, Mata JP, de Campo L, Rehm C, Hill AJ, Dutta NK. Evolution of the interfacial structure of a catalyst ink with the quality of the dispersing solvent: a contrast variation small-angle and ultrasmall-angle neutron scattering investigation. ACS Appl Mater Interfaces 2019;11(10):9934–46.
[19] Mehrazi S, Sarker M, Mojica F, Rolfe P, Chuang P-YA. A rheological approach to studying process-induced structural evolution of the microporous layer in a proton exchange membrane fuel cell. Electrochim Acta 2021;138690.
[20] Aldebert P, Dreyfus B, Gebel G, Nakamura N, Pineri M, Volino F. Rod like micellar structures in perfluorinated ionomer solutions. J Physique 1988;49(12):2101–9.
[21] Aldebert P, Dreyfus B, Pineri M. Small-angle neutron scattering of perfluorosulfonated ionomers in solution. Macromolecules 1986;19(10):2651–3.
[22] Takahashi S, Mashio T, Horibe N, Akizuki K, Ohma A. Analysis of the microstructure formation process and its influence on the performance of polymer electrolyte fuel-cell catalyst layers. ChemElectroChem 2015;2(10):1560–7.
[23] Kudo K, Jinnouchi R, Morimoto Y. Humidity and temperature dependences of oxygen transport resistance of nafion thin film on platinum electrode. Electrochim Acta 2016;209:682–90.
[24] Wu J, Yuan XZ, Wang H, Blanco M, Martin JJ, Zhang J. Diagnostic tools in PEM fuel cell research: Part II: Physical/chemical methods. Int J Hydrogen Energy 2008;33(6):1747–57.
[25] Soboleva T, Malek K, Xie Z, Navessin T, Holdcroft S. PEMFC catalyst layers: the role of micropores and mesopores on water sorption and fuel cell activity. ACS Appl Mater Interfaces 2011;3(6):1827–37.
[26] Yang F, Xin L, Uzunoglu A, Qiu Y, Stanciu L, Ilavsky J, Li W, Xie J. Investigation of the interaction between nafion ionomer and surface functionalized carbon black using both ultrasmall angle X-ray scattering and cryo-TEM. ACS Appl Mater Interfaces 2017;9(7):6530–8.
[27] Khandavalli S, Park JH, Kariuki NN, Myers DJ, Stickel JJ, Hurst K, Neyerlin KC, Ulsh M, Mauger SA. Rheological Investigation on the Microstructure of Fuel Cell Catalyst Inks. ACS Appl Mater Interfaces 2018;10(50):43610–22.
[28] Lyu X, Van Cleve T, Young E, Li J, Yu H, Cullen DA, Neyerlin K, Serov A. Design of graded cathode catalyst layers with various ionomers for fuel cell application. J Power Sources 2023;556:232530.
[29] Creel EB, Tjiptowidjojo K, Lee JA, Livingston KM, Schunk PR, Bell NS, Serov A, Wood III DL. Slot-die-coating operability windows for polymer electrolyte membrane fuel cell cathode catalyst layers. J Colloid Interface Sci 2022;610:474–85.
[30] Du S, Guan S, Mehrazi S, Zhou F, Pan M, Zhang R, Chuang P-YA, Sui P-C. Effect of dispersion method and catalyst on the crack morphology and performance of catalyst layer of PEMFC. J Electrochem Soc 2021;168(11):114506.
[31] Dixit MB, Harkey BA, Shen F, Hatzell KB. Catalyst layer ink interactions that affect coatability. J Electrochem Soc 2018;165(5):F264.
[32] Guo Y, Yang D, Li B, Yang D, Ming P, Zhang C. Effect of dispersion solvents and ionomers on the rheology of catalyst inks and catalyst layer structure for proton exchange membrane fuel cells. ACS Appl Mater Interfaces 2021;13(23):27119–28.
[33] Narayanan A, Mugele F, Duits MH. Mechanical history dependence in carbon black suspensions for flow batteries: A rheo-impedance study. Langmuir 2017;33(7):1629–38.
[34] Narayanan A, Wijnperlé D, Mugele F, Buchholz D, Vaalma C, Dou X, Passerini S, Duits M. Influence of electrochemical cycling on the rheo-impedance of anolytes for Li-based semi solid flow batteries. Electrochim Acta 2017;251:388–95.
[35] Brilloni A, Poli F, Spina GE, Genovese D, Pagnotta G, Soavi F. Improving the electrical percolating network of carbonaceous slurries by superconcentrated electrolytes: an electrochemical impedance spectroscopy study. ACS Appl Mater Interfaces 2021;13(11):13872–82.
[36] Liu Q, Richards JJ. Rheo-electric measurements of carbon black suspensions containing polyvinylidene difluoride in N-methyl-2-pyrrolidone. J Rheol 2023;67(3):647–59.
[37] Helal A, Divoux T, McKinley GH. Simultaneous rheoelectric measurements of strongly conductive complex fluids. Phys Rev A 2016;6(6):064004.
[38] Doppelhammer N, Pellens N, Martens J, Kirschhock CE, Jakoby B, Reichel EK. Moving electrode impedance spectroscopy for accurate conductivity measurements of corrosive ionic media. ACS Sens 2020;5(11):3392–7.
[39] Tadros TF. Rheology of dispersions: principles and applications. 2010.
[40] Yang D, Zhu S, Guo Y, Tang H, Yang D, Zhang C, Ming P, Li B. Control of cluster structures in catalyst inks by a dispersion medium. ACS Omega 2021;6(48):32960–9.
[41] Torbati-Sarraf H, Ding L, Khakpour I, Poursaee A. Electrochemical impedance spectroscopic analyses of the influence of the surface nanocrystallization on the passivation of carbon steel in the pore solution. J Mater Civ Eng 2021;33(1):04020419.
[42] Petek TJ, Hoyt NC, Savinell RF, Wainright JS. Characterizing slurry electrodes using electrochemical impedance spectroscopy. J Electrochem Soc 2015;163(1):A5001.
[43] Shukla S, Bhattacharjee S, Weber AZ, Secanell M. Experimental and theoretical analysis of ink dispersion stability for polymer electrolyte fuel cell applications. J Electrochem Soc 2017;164(6):F600–9.
[44] Mehrazi S, Sarker M, Chuang P-YA. Effect of high aspect ratio additives on microstructural and mass transport properties of the microporous layer in a proton exchange membrane fuel cell. J Power Sources 2023;580:233361.
[45] Meslam M, Elzatahry AA, Youssry M. Promising aqueous dispersions of carbon black for semisolid flow battery application. Colloids Surf A 2022;129376.
[46] Ren H, Teng Y, Meng X, Fang D, Huang H, Geng J, Shao Z. Ionomer network of catalyst layers for proton exchange membrane fuel cell. J Power Sources 2021;506:230186.

[47] Lee H, Koo S. Analysis of fractal aggregates in a colloidal suspension of carbon black from its sedimentation and viscosity behavior. Korea-Aust Rheol J 2016;28(4):267–73.
[48] Takahashi S, Shimanuki J, Mashio T, Ohma A, Tohma H, Ishihara A, Ito Y, Nishino Y, Miyazawa A. Observation of ionomer in catalyst ink of polymer electrolyte fuel cell using cryogenic transmission electron microscopy. Electrochim Acta 2017;224:178–85.
[49] Xu F, Zhang H, Ilavsky J, Stanciu L, Ho D, Justice MJ, Petrache HI, Xie J. Investigation of a catalyst ink dispersion using both ultra-small-angle X-ray scattering and cryogenic TEM. Langmuir 2010;26(24):19199–208.
[50] Chuang P-YA, Rahman MA, Mojica F, Hussey DS, Jacobson DL, LaManna JM. The interactive effect of heat and mass transport on water condensation in the gas diffusion layer of a proton exchange membrane fuel cell. J Power Sources 2020;480:229121.
[51] Ohma A, Fushinobu K, Okazaki K. Influence of Nafion® film on oxygen reduction reaction and hydrogen peroxide formation on pt electrode for proton exchange membrane fuel cell. Electrochim Acta 2010;55(28):8829–38.
[52] Nonoyama N, Okazaki S, Weber AZ, Ikogi Y, Yoshida T. Analysis of oxygen-transport diffusion resistance in proton-exchange-membrane fuel cells. J Electrochem Soc 2011;158(4):B416.
[53] Wen Z, Li S, Yi S, Zhao Q, Zhu Z, Pan M. Optimization of the ionomer-to-carbon ratio in the cathode catalyst layer of PtCoMn/C alloy catalysts. Int J Electrochem Sci 2023;18(6):100152.
[54] Schneider P, Scherzer A-C, Storey BD, Klingele M, Zamel N, Gerteisen D. The effect of ionomer to carbon ratio and relative humidity on cathode catalyst degradation in PEM fuel cells. J Electrochem Soc 2023;170(10):104505.
[55] Kakinuma K, Kawamoto M, Tamoto K, Yamaguchi M, Honmura S, Iiyama A, Uchida M. Evaluation of ionomer distribution on electrocatalysts for polymer electrolyte fuel cells by use of a low acceleration voltage scanning electron microscope. J Electrochem Soc 2021;168(5):054510.
[56] Makharia R, Mathias MF, Baker DR. Measurement of catalyst layer electrolyte resistance in PEFCs using electrochemical impedance spectroscopy. J Electrochem Soc 2005;152(5):A970.
[57] Yakovlev YV, Lobko YV, Vorokhta M, Nováková J, Mazur M, Matolínová I, Matolín V. Ionomer content effect on charge and gas transport in the cathode catalyst layer of proton-exchange membrane fuel cells. J Power Sources 2021;490:229531.